Soft Matter

PAPER

Check for updates

Construction of dendritic Janus nanomotors with H_2O_2 and NIR light dual-propulsion *via* a Pickering emulsion†

Haozheng Lv, Yi Xing, Xin Du, [iD] * Tailin Xu [iD] * and Xueji Zhang [iD]

Artificial micro/nanomotors with a dual-propulsion property have attracted considerable attention recently due to their attractive performances in complex fluidic environments. In this work, we successfully constructed Janus nanomotors with H_2O_2 and NIR light dual-propulsion by employing dendritic porous silica nanoparticles (DPSNs) as carriers *via* a Pickering emulsion and electrostatic self-assembly. The aminopropyl-modified DPSNs (DPSNs-NH_2) with positive charge were semiburied in paraffin wax microparticles in order to achieve electrostatic adsorption of Pt nanoparticles (NPs) with negative charge on the exposed surface for H_2O_2 propulsion, followed by electrostatic adsorption of negatively charged CuS NPs with excellent NIR light absorption on the other exposed surface of the eluted DPSNs-NH_2@Pt for NIR light propulsion. Center-radial large mesopores facilitate the high density loading of Pt NPs and CuS NPs for efficient propulsion. Compared with the commonly used sputtering approach, this Pickering emulsion method can realize relatively large-scale fabrication of Janus NPs. DPSNs-NH_2@Pt@CuS Janus nanomotors can be effectively driven not only by self-diffusiophoresis, which results from the decomposition of H_2O_2 catalyzed by Pt NPs, but also by self-thermophoresis, which is generated from thermal gradients caused by the photothermal effect of CuS NPs. Moreover, the motion speed of the nanomotors can be conveniently modulated by regulating the H_2O_2 concentration and NIR light intensity. This work provides a novel exploration into the construction of dual-propulsion nanomotors, which are supposed to have significant potential in biomedical and intelligent device applications.

1. Introduction

Recently, artificial micro/nanomotors, which are capable of effectively converting diverse energy sources into autonomous movement, have attracted tremendous attention in completing sophisticated tasks including active cargo delivery, cell manipulation, biosensing, environmental remediation, *etc.*[1–9] The micro/nanomotors can be powered by chemical fuel, light,[1–3,10–12] ultrasound,[13,14] and magnetic fields.[15–17] Traditionally, a micro/nanomotor can be propelled by only a single chemical or physical stimulus propulsion mode. Nevertheless, it might suffer from restrictions in energy resource and environmental factors. For instance, the inherent toxicity and incomplete degradation of H_2O_2 may restrict the applicability of these micro/nanomotors in the biomedical field, while physical propulsion modes may have some disadvantages, such as scalability issues and the requirement of intricate driving systems. The optimal working conditions and potential applications largely depend on the extraordinarily different nature of the chemical and physical stimuli.

Dual-propulsion micro/nanomotors integrating two kinds of different propulsion modes into a single nanoscale device have been extensively explored, including chemical-magnetic, light-magnetic, chemical-ultrasound, light-chemical and so on.[18–28] This dual-propulsion mode of hybrid artificial micro/nanomotors increases the versatility and expands the scope of operation of nanoscale vehicles compared to those based on a single propulsion mode. Nevertheless, these micro/nanomotors always employ smooth-faced micro/nanospheres or nanotubes as nanoplatform carriers, which may result in a low loading capacity for further cargo delivery application. Recently, novel dendritic porous silica nanoparticles (DPSNs) with highly accessible pore surfaces have been fabricated.[29–33] Compared with conventional smooth-faced micro/nanospheres, DPSNs have unique three-dimensional superstructures with many permeable center-radial large pore channels and high pore volumes for high

Research Center for Bioengineering and Sensing Technology, Beijing Key Laboratory for Bioengineering and Sensing Technology, Department of Chemistry & Biological Engineering, University of Science & Technology Beijing, Beijing 100083, P. R. China. E-mail: duxin@ustb.edu.cn, xutailin@ustb.edu.cn
† Electronic supplementary information (ESI) available. See DOI: 10.1039/d0sm00552e

loading capacities,[29–33] which should make them an ideal carrier to build artificial micro/nanomotors.

In recent years, a feasible Pickering emulsion strategy to fabricate Janus particles by using colloidal particles to stabilize wax-in-water emulsions has emerged.[34–36] The main advantage is that large-scale Janus silica NPs with controllable diameters can be fabricated in a simple way. The molten wax in the emulsions is solidified when it is cooled to room temperature, leading to the locking of the silica NPs at the surface of the wax microparticles. When captured by the interface of solid/liquid, the silica NPs cannot move and their exposed part to the aqueous phase can be further subjected to chemical modification or physical adsorption. However, to the best of our knowledge, there are few reports taking advantage of DPSNs as a colloidal stabilizer in the Pickering emulsion method.

Herein, we designed dual-powered DPSNs-NH$_2$@Pt@CuS Janus nanomotors, which can be propelled by the decomposition of H$_2$O$_2$ and NIR light irradiation. Such Janus nanomotors were fabricated based on a Pickering emulsion by employing the aminopropyl-modified DPSNs (DPSNs-NH$_2$) as the stabilizer. On the one hand, the Janus nanomotors can be propelled by the decomposition of H$_2$O$_2$ that is catalyzed by Pt NPs. On the other hand, the hemispherical distribution of CuS NPs, which have a high photothermal conversion efficiency,[37–41] can generate asymmetrical self-thermophoresis under NIR light irradiation, resulting in NIR light-propulsion. Such a design provides an alternative strategy to construct advanced dual-propulsion nanomotors, which may have promising applications.

2. Materials and methods

2.1 Chemicals and characterization methods are listed in the ESI†

2.2 Synthesis of wax@DPSNs-NH$_2$ particles by the Pickering emulsion method

DPSNs-NH$_2$ (50 mg), sodium dodecylsulfate (7.1 mg) and water (10 mL) were first sonicated together for 15 min. Then, the mixture was stirred at a speed of 600 rpm (75 °C) and paraffin wax (1.1 g) was slowly added. When the wax was completely melted, the mixture was rapidly stirred at a speed of 1000 rpm at 75 °C for another 2 h. Then, the heating and stirring of the emulsion were stopped and it was allowed to cool to room temperature, solidifying the wax, after which the solid phase was filtered and washed in ethanol.

2.3 Synthesis of DPSNs-NH$_2$@Pt Janus NPs

20 mg of the as-prepared wax@DPSNs-NH$_2$ particles and 4 mL of ethanol were first added into a 20 mL capped vial, followed by adding an excessive amount of negatively charged Pt NPs (4 mL, 0.247 mmol L^{-1}) suspension for saturation adsorption of Pt NPs on the exposed surface of DPSNs-NH$_2$.[32,33] After the mixture was gently agitated for 30 min at room temperature, wax@DPSNs-NH$_2$@Pt was obtained by centrifugation and washed with pure water and ethanol several times. Finally, DPSNs-NH$_2$@Pt Janus NPs were released from wax@DPSNs-NH$_2$@Pt by

dispersion in trichloromethane followed by centrifugation. The obtained precipitate was stored in ethanol for further use.

2.4 Synthesis of DPSNs-NH$_2$@Pt@CuS Janus NPs

The above-mentioned DPSNs-NH$_2$@Pt Janus NP suspension was treated with ultrasonication at a power of 300 W for 30 min. Then, 200 μL of DPSNs-NH$_2$@Pt suspension was added into an excessive amount of negatively charged CuS NP (1 mL, 0.997 mmol L^{-1}) suspension for saturation adsorption of CuS NPs on the exposed surface of DPSNs-NH$_2$@Pt in a 2.5 mL centrifuge tube,[32,33] followed by stirring for 30 min at room temperature. The asymmetric DPSNs-NH$_2$@Pt@CuS Janus NPs were obtained by centrifugation and washed with water three times.

2.5 Characterization of H$_2$O$_2$ propulsion

Hydrogen peroxide (H$_2$O$_2$) solutions with different mass fractions ranging from 0 to 6% were prepared as chemical fuel. A small amount of the fabricated DPSNs-NH$_2$@Pt@CuS Janus NPs was dispersed in deionized water and sonicated for 30 min at an ultrasonic power of 300 W. Then, the suspension was diluted to an appropriate concentration that should favour observation of the motion of DPSNs-NH$_2$@Pt@CuS Janus NPs. 50 μL of the diluted suspension and 50 μL of the as-prepared H$_2$O$_2$ solutions were first uniformly mixed in a 2.5 mL centrifuge tube. Subsequently, the mixture was added into the groove of a quartz glass slide and sealed with a highly-clean cover glass to avoid gas disturbances. We used a dark field microscope to observe the motion of particles (resolution: particle size of over 100 nm), so there is no need for fluorescent dye labeling on the particle surface. All the imaging experiments were recorded at a rate of 10–12.5 frames per second using a Nikon upright microscope, which was equipped with a 100 W halogen tungsten lamp, an oil immersion dark field condenser (NA 1.20–1.43), a 40×/20× plan fluor objective, and a color charge coupled device camera (DP73, Olympus, Japan). ImageJ and its plugin (MTrackJ) were conjunctively used to analyze the motion of the nanomotors. By counting the number of clear particles in a frame of video, we calculated that the concentration of nanomotors is about 3.19×10^{-5} μm^2.

2.6 Characterization of NIR light propulsion

The above-mentioned diluted suspension was added into the groove of the quartz glass slide and sealed with a highly-clean cover glass to avoid gas disturbances. A Laser Beam Expander of NIR light device (wavelength: 980 nm) was fixed in the same horizontal plane of the quartz glass slide. After shining the red indicator light for 10 s, the NIR light switch was turned on to trigger the motion, and the motion frames were recorded for another 20 s with different NIR light irradiation power (0, 1, 2 and 3 W). All the imaging experiments were recorded at a rate of 10–12.5 frames per second using a Nikon upright microscope, which was equipped with a 100 W halogen tungsten lamp, an oil immersion dark field condenser (NA 1.20–1.43), a 40×/20× plan fluor objective, and a color charge coupled device camera

(DP73, Olympus, Japan). ImageJ and its plugin (MTrackJ) were conjunctively used to analyze the motion of the nanomotors.

3. Results and discussion

As exhibited in the schematic illustration in Fig. 1, the DPSNs-NH_2@Pt@CuS Janus nanomotor was synthesized *via* a Pickering emulsion method combined with electrostatic self-assembly. The fabrication process mainly contains five steps: (1) the synthesis of DPSNs and the post-grafting of aminopropyl groups on the surface of the center-radial pores of DPSNs to form aminopropyl-modified DPSNs (DPSNs-NH_2) with a positive charge, (2) the partial embedding of DPSNs-NH_2 into wax microparticles (wax@DPSNs-NH_2) *via* a Pickering emulsion technique (Fig. S1, ESI†), (3) the electrostatic adsorption of negatively charged Pt NPs on the exposed surface of DPSNs-NH_2
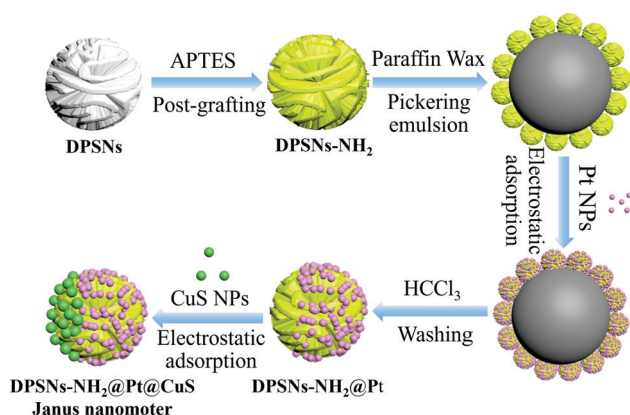

Fig. 1 Schematic illustration of the synthesis process of the DPSNs-NH_2@Pt@CuS Janus nanomotors, which are equipped with asymmetric distributions of Pt NPs on one side and CuS NPs on the other side of the DPSNs-NH_2 *via* a Pickering emulsion method combined with electrostatic adsorption between positively charged DPSNs-NH_2 and negatively charged Pt NPs/CuS NPs.
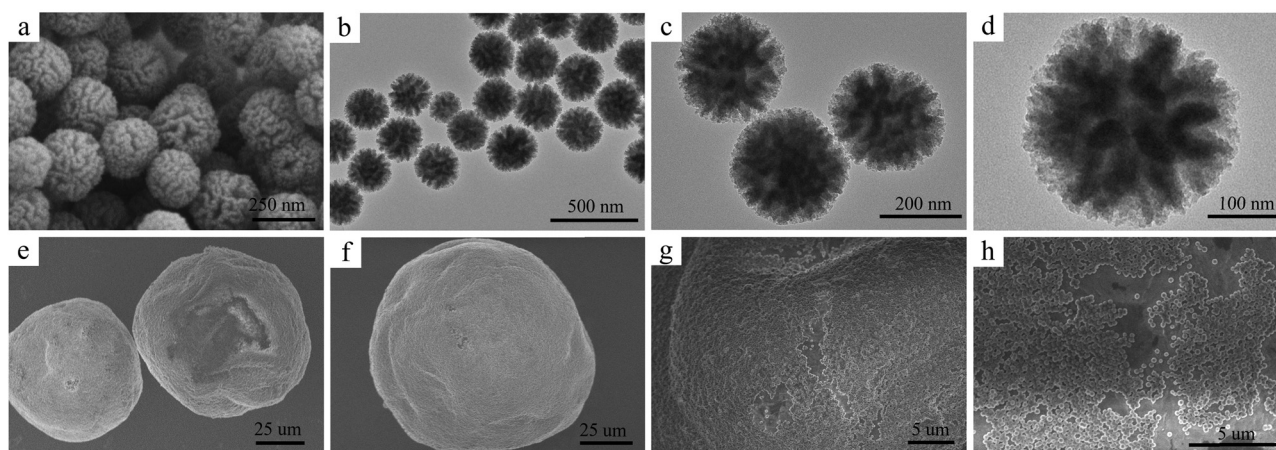
partially embedded into the wax microparticles (wax@DPSNs-NH_2@Pt), (4) the formation of Janus DPSNs-NH_2@Pt by washing wax@DPSNs-NH_2@Pt with $HCCl_3$, and (5) the electrostatic adsorption of negatively charged CuS NPs on the exposed surface of DPSNs-NH_2@Pt to form the DPSNs-NH_2@Pt@CuS Janus nanomotor. Noteworthily, instead of particles with a smooth surface, for the first time, DPSNs with center-radial large pores are first employed as a stabilizer in a Pickering emulsion in order to achieve the high adsorption/loading of Pt and CuS NPs.

As shown in Fig. 2a–d, SEM and TEM images show that the fabricated DPSNs possess a uniform particle size (256 ± 30 nm, *i.e.*, *ca.* 250 nm) and dendritic-like large center-radial pores (particle surface pore sizes: 25 ± 10 nm). The N_2 adsorption–desorption result exhibits a type IV isotherm, suggesting the existence of mesopores. Brunauer–Emmett–Teller (BET) analysis shows that the DPSNs have a specific surface area of 281 m^2 g^{-1} and a total pore volume of 0.93 cm^3 g^{-1}. After aminopropyl-modification, the zeta potential varies from -20.7 mV (DPSNs) to $+39.1$ mV (DPSNs-NH_2) (Fig. S2, ESI†), but the particle morphology and structure show little change. SEM images in Fig. 2e–h show the morphology of wax@DPSNs-NH_2 obtained from the Pickering emulsion method. The solid wax microparticles with the particle size of *ca.* 100 μm contain a densely packed arrangement of DPSNs-NH_2 partially embedded into their surface after washing with a suitable amount of ethanol and water. Moreover, the majority of DPSNs-NH_2 are locked on the surface of the wax sphere in the form of a monolayer, which is a basic and important step for the consequent asymmetric adsorption of Pt NPs on the exposed surface of the microparticles. However, when the wax@DPSNs-NH_2 sample was washed with excessive ethanol during the filtration step, it removes some DPSNs-NH_2 embedded onto the surface of the solid wax microparticles (Fig. S3, ESI†). Subsequently, citrate-stabilized Pt NPs with a particle size of 3.3 ± 0.6 nm and a zeta potential of -33.4 mV were synthesized (Fig. S4a and b, ESI†) and assembled on the exposed part of DPSNs-NH_2. TEM images in Fig. 3a–d show that

Fig. 2 (a) SEM and (b–d) TEM images of DPSNs-NH_2 with the particle size of *ca.* 250 nm and center-radial large pores (surface pore size: *ca.* 25 ± 10 nm). (e–h) SEM images of spherical wax-DPSNs-NH_2, which are formed from wax microparticles with a layer of DPSNs-NH_2 partially embedded into them.
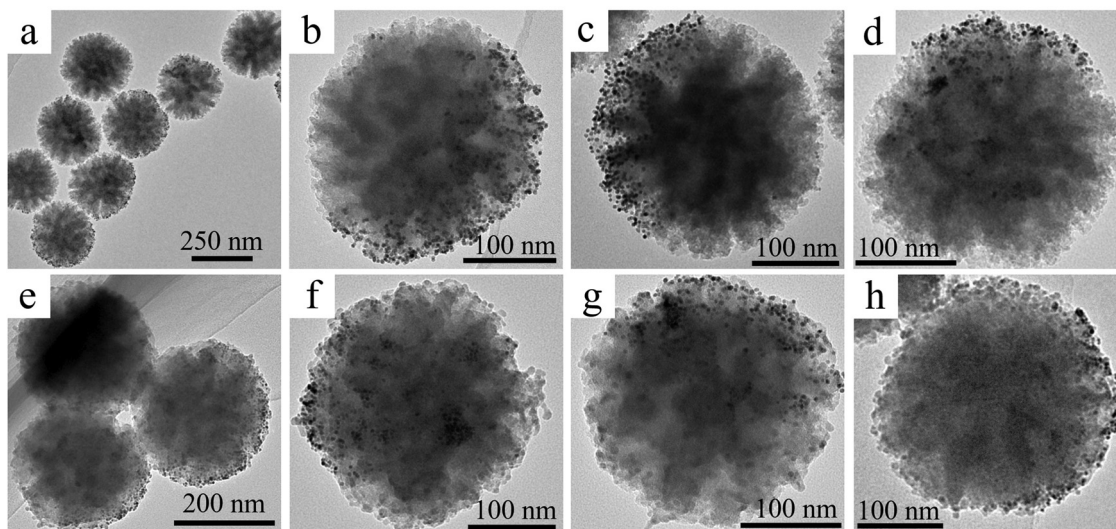
Fig. 3 TEM images (a–d) of DPSNs-NH$_2$@Pt Janus NPs in which positively charged DPSNs-NH$_2$ are partially covered by negatively charged Pt NPs through electrostatic interaction. (e–h) TEM images of DPSNs-NH$_2$@Pt@CuS Janus NPs, which are fabricated by the electrostatic self-assembly process between DPSNs-NH$_2$@Pt Janus NPs and CuS NPs.

the synthesized DPSNs-NH$_2$@Pt Janus NPs possess the characteristics that Pt NPs were only uniformly loaded on the center-radial pore surface of the unprotected part of DPSNs-NH$_2$ *via* electrostatic adsorption. Moreover, citrate-stabilized CuS NPs with a particle size of 7.8 ± 1.9 nm and a zeta potential of −28.6 mV were also prepared (Fig. S4c and d, ESI†) and assembled on the exposed part of DPSNs-NH$_2$@Pt Janus NPs. TEM images in Fig. 3e–h exhibit the Janus spatial distribution of Pt NPs and CuS NPs on the surface of DPSNs-NH$_2$, indicating their successful construction. The UV-vis-NIR adsorption spectra of DPSNs-NH$_2$@Pt@CuS NPs dispersed in water show a weak wide peak in the wavelength range of 800–1000 nm and an absorbance rise at the wavelength of 600 nm (Fig. S5, ESI†), which are ascribed to the adsorption of Pt and CuS NPs (Fig. S6, ESI†), respectively. Thus, this also suggests the successful fabrication of DPSNs-NH$_2$@Pt@CuS NPs. It is worth noting that the different coverage proportions of Pt NPs or CuS NPs on DPSNs-NH$_2$ should be attributed to the embedded depth of DPSNs-NH$_2$ on the wax microparticles, which can be controlled by precisely tuning the experimental parameters.[34–36]

The asymmetric distribution of Pt NPs, which is a common catalyst for the non-electrochemical decomposition of H$_2$O$_2$ into H$_2$O and oxygen, allows us to explore the self-diffusiophoresis property of DPSNs-NH$_2$@Pt@CuS NPs. As illustrated in Fig. 4a, the cause of H$_2$O$_2$-driven propulsion is the concentration gradient of oxygen molecules that is derived from the decomposition of H$_2$O$_2$ catalyzed by the asymmetrically loaded Pt NPs on DPSNs-NH$_2$@Pt@CuS NPs. The length of non-directional trajectory (Fig. 4b) of DPSNs-NH$_2$@Pt@CuS NPs exhibits a positive correlation with the increase of H$_2$O$_2$ concentration from 0 to 3 wt% (Video S1, ESI†). The particles in the suspensions are constantly impacted by the liquid molecules and will not stay in a fixed position. The particles move constantly and their positions are different at each moment. The mean square displacement (MSD)

of the particle at time t can be calculated. MSD = $\langle |r(t) - r(0)|^2 \rangle$. The plots of MSD in Fig. 4c display an increasing tendency *versus* time interval (Δt). The straight lines of the MSD indicate the non-directional movement. The higher the concentration of H$_2$O$_2$, the more enhanced the self-propulsion of DPSNs-NH$_2$@Pt@CuS NPs realized when the statistic time (*ca.* 0.1 s) is longer than the rotational diffusion time (*ca.* 0.01 s for 250 nm particles). DPSNs-NH$_2$@Pt@CuS Janus nanomotors are effectively propelled by H$_2$O$_2$, which can be further demonstrated by the fact that the baseline of instantaneous velocity of DPSNs-NH$_2$@Pt@CuS NPs in 3 wt% H$_2$O$_2$ is about twice that in 0 wt% H$_2$O$_2$ (*i.e.*, the instantaneous velocity of Brownian motion) (Fig. 4d). It should be noted that the instantaneous velocities are only used for comparative purposes, and they should not be mistaken for virtual velocities because the measure of the velocity of Brownian motion requires very complex and dedicated experiments. Also, the H$_2$O$_2$-driven average velocity of DPSNs-NH$_2$@Pt@CuS NPs gradually increases with the higher concentration of H$_2$O$_2$ to some extent, as shown in Fig. 4e. The diffusion coefficient (D_L) is the mass or moles of a substance diffused vertically through a unit area along the diffusion direction under the condition of unit concentration gradient per unit time. The D_L of both DPSNs-NH$_2$@Pt NPs and DPSNs-NH$_2$@Pt@CuS NPs can be calculated by the equation D_L = MSD/(4·Δt) (Fig. 4f). The D_L of the Brownian motion of DPSNs-NH$_2$@Pt@CuS NPs is measured to be *ca.* 1.1 μm^2 s^{-1} in water without H$_2$O$_2$ addition, which is lower than the value 1.72 μm^2 s^{-1} calculated from the Stokes–Einstein equation for the nanomotor whose size is 250 nm. The reason for this is that the hydrated particle size is bigger than the real size measured from TEM images. In addition, the adsorption of both Pt NPs and CuS NPs to DPSNs can also lead to an increase of particle diameter, which similarly contributes to the reduction of actual D_L value. Compared with the Brownian movement in the absence of H$_2$O$_2$, the D_L of DPSNs-NH$_2$@Pt@CuS NPs is enhanced
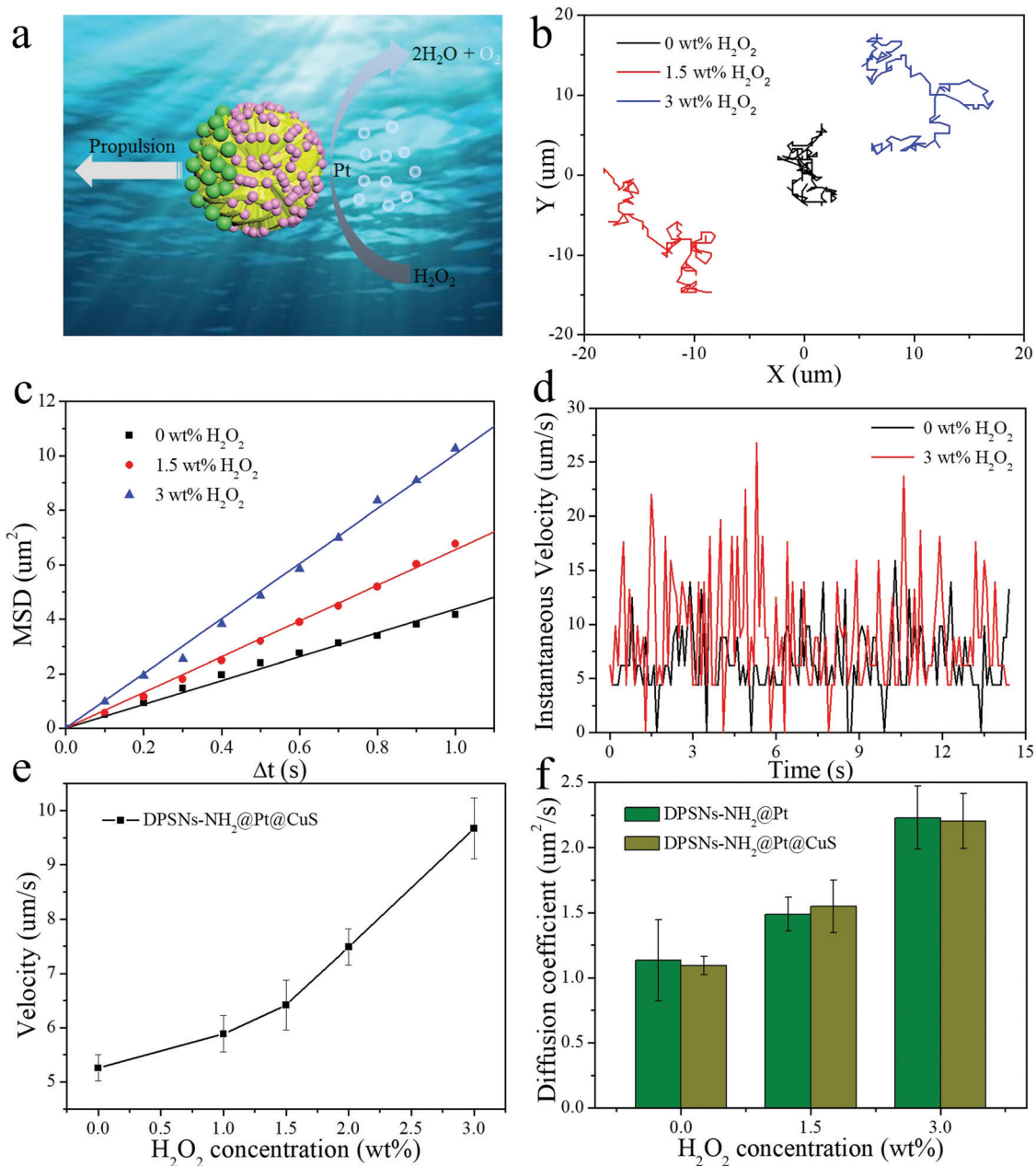
Fig. 4 (a) Schematic illustration of the propulsion mechanism of H_2O_2-driven DPSNs-NH_2@Pt@CuS Janus nanomotors. (b) Trajectories of DPSNs-NH_2@Pt@CuS Janus nanomotors at different H_2O_2 concentrations (15 s). (c) Fitting plot of MSD of DPSNs-NH_2@Pt@CuS *versus* time interval (*t*) at different H_2O_2 concentrations. (d) Instantaneous velocity of DPSNs-NH_2@Pt@CuS Janus nanomotors at different H_2O_2 concentrations of 0 and 3 wt% (15 s). (e) Dependence of average velocity of DPSNs-NH_2@Pt@CuS on different H_2O_2 concentrations. (f) Diffusion coefficient of DPSNs-NH_2@Pt and DPSNs-NH_2@Pt@CuS at different H_2O_2 concentrations, respectively.

to be 1.5 and 2.2 μm^2 s^{-1} for 1.5 and 3 wt% H_2O_2, respectively. The D_L of DPSNs-NH_2@Pt@CuS nanomotors is even enhanced up to 100% in 3 wt% H_2O_2 compared to their Brownian motion. Due to the high rotational diffusion coefficient of the nanoparticles, the H_2O_2 propulsion can only enhance Brownian motion. Moreover, almost the same D_L value for DPSNs-NH_2@Pt and DPSNs-NH_2@Pt@CuS at different H_2O_2 concentrations further demonstrates that only Pt NPs play a decisive role in H_2O_2-propulsion (Fig. 4f). It has been found in our previous report that the values of D_L and average velocity of DPSNs-NH_2@Pt-50% were higher than

those of smooth silica nanospheres-NH_2@Pt-50% at the same concentration of H_2O_2, which was ascribed to the loading of more Pt NPs, thus increasing the catalytic activity.[33]

Apart from the motion driven by different concentrations of H_2O_2, the other excellent property of the DPSNs-NH_2@Pt@CuS NPs is the self-thermophoresis propulsion by the photothermal effect provided by the CuS NPs. Here, the UV-vis-NIR spectra of DPSNs-NH_2@Pt@CuS NPs revealed a surface plasmon resonance (SPR) peak at about 980 nm, which is consistent with the characteristic absorption peak of CuS (Fig. S6c, ESI†).

The high absorption is very important for photothermal conversion in the NIR region. Hence, when exposed to a NIR laser, a localized photothermal effect on the CuS covered part leads to the formation of thermal gradients across the DPSNs-NH$_2$@Pt@CuS NPs, thus propelling the DPSNs-NH$_2$@Pt@CuS nanomotors by self-thermophoresis (Fig. 5a). Compared with the Brownian motion of DPSNs-NH$_2$@Pt@CuS NPs without the NIR irradiation, trajectory lengths became more stretched and prolonged with the increased power of NIR light and they were recorded over a period of the first 10 s without NIR irradiation and over the next 20 s under NIR irradiation (Fig. 5b). The trajectory length of DPSNs-NH$_2$@Pt@CuS Janus nanomotors enhanced slightly to only 89 μm in 20 s under the irradiation of

1 W. However, under 3 W of NIR light irradiation, the trajectory of DPSNs-NH$_2$@Pt@CuS NPs was even increased to 134 μm in 20 s. The movement directionality of DPSNs-NH$_2$@Pt@CuS nanomotors is due to the directionality of NIR light laser. Due to the strong SPR absorption of the CuS NPs in the NIR region, thermophoretic force along DPSNs-NH$_2$@Pt@CuS produces a net resultant force, which can overcome strong Brownian forces and thus induce rapid motion of the nanomotors. MSD curves in Fig. 5c fit the equation MSD = $4D·\Delta t + v^2·\Delta t^2$ very well. The propulsive velocity of DPSNs-NH$_2$@Pt@CuS NPs increases to 4.07 μm s^{-1} under 3 W of NIR light irradiation, much higher than that (1.46 μm s^{-1}) under 1 W. The diffusion coefficient of DPSNs-NH$_2$@Pt@CuS NPs under NIR irradiation
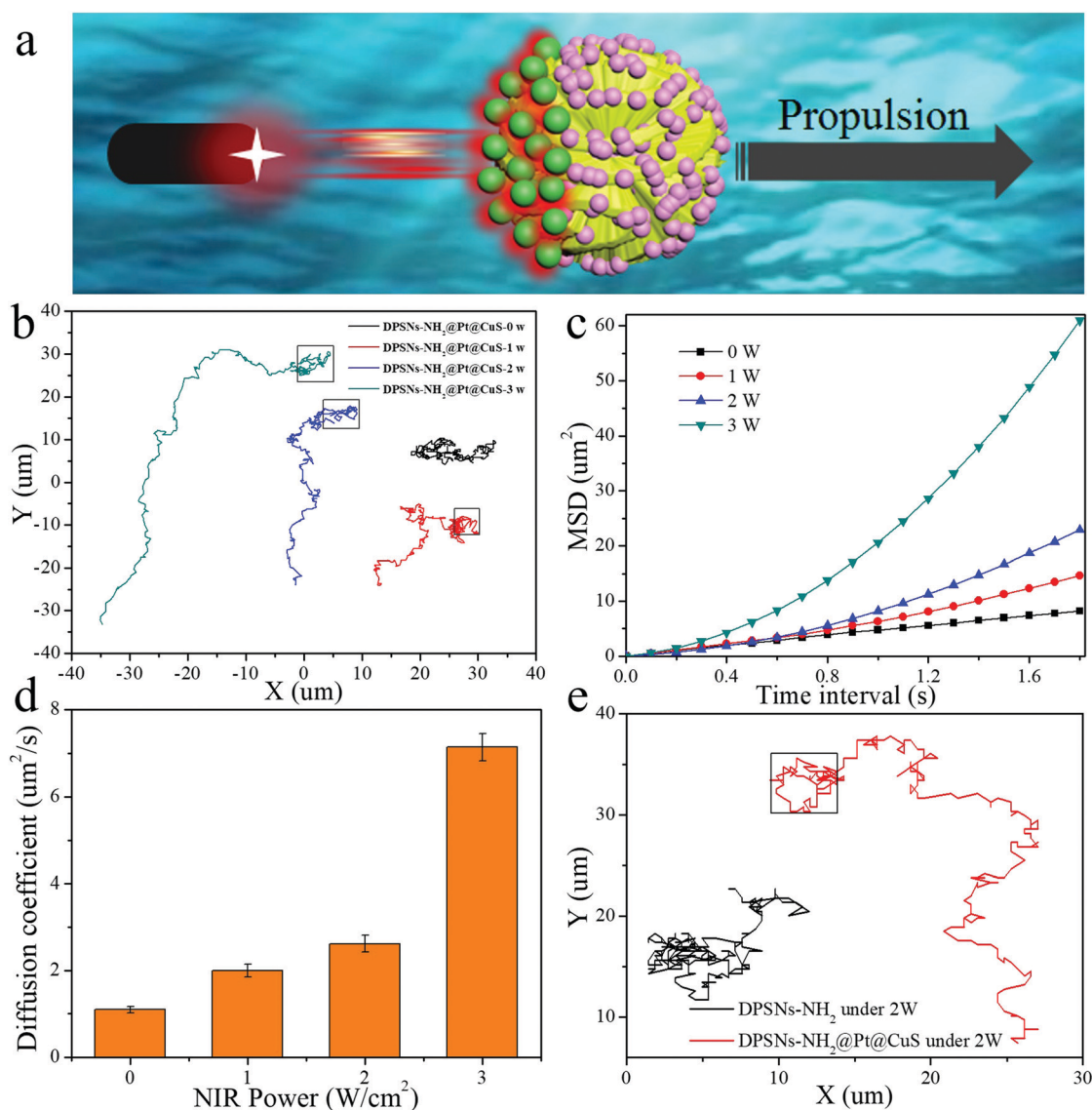

Fig. 5 (a) Schematic illustration of light-driven DPSNs-NH$_2$@Pt@CuS Janus nanomotors under NIR laser irradiation. (b) Trajectories of DPSNs-NH$_2$@Pt@CuS Janus nanomotors with light of different power in 30 s, the signed part of the trajectory by black wireframe indicates the Brownian motion in the first 10 s without NIR irradiation. (c) Fitting plot of MSD of DPSNs-NH$_2$@Pt@CuS *versus* time interval (*t*) under NIR irradiation with different power. (d) Diffusion coefficient of DPSNs-NH$_2$@Pt@CuS under NIR irradiation with different power. (e) Trajectories of DPSNs-NH$_2$ and DPSNs-NH$_2$@Pt@CuS Janus nanomotors with the NIR light irradiation of 2 W in 30 s, the signed part of the trajectory by a black wireframe indicates the Brownian motion in the first 10 s without NIR irradiation.

with different power is shown in Fig. 5d and it improved with the increase of NIR power density. Compared with the Brownian motion in the absence of NIR light, the diffusion coefficient of DPSNs-NH$_2$@Pt@CuS NPs is significantly increased to 7.2 μm^2 s^{-1} under 3 W of NIR light irradiation, indicating that the enhanced propulsion was achieved by the thermophoretic mechanism under NIR light irradiation. Furthermore, we also studied the propulsion situation of both bare DPSNs-NH$_2$ and DPSNs-NH$_2$@Pt@CuS NPs under the same NIR light irradiation of 2 W as a control experiment. As recorded in Fig. 5e, the trajectories of DPSNs-NH$_2$@Pt@CuS NPs were prolonged a lot compared to that of DPSNs-NH$_2$, which demonstrates that the NIR irradiation can effectively activate the diffusion of Janus nanomotors due to the photothermal effect (Video S2, ESI†).

4. Conclusion

In conclusion, we successfully fabricated DPSNs-NH$_2$@Pt@CuS Janus nanomotors with H$_2$O$_2$ and NIR light dual-propulsion *via* a Pickering emulsion combined with electrostatic self-assembly method. The motion speed of Janus nanomotors can be enhanced not only by self-diffusiophoresis due to the decomposition of H$_2$O$_2$ catalyzed by Pt NPs, but also by self-thermophoresis owing to thermal gradients caused by the photothermal effect of CuS NPs. Furthermore, we can conveniently modulate the motion speed of Janus nanomotors by controlling H$_2$O$_2$ concentration and NIR light power. This work provides a new approach to construct dual-propulsion nanomotors by the asymmetric adsorption of various functional NPs. It is expected that this kind of Janus nanomotors will act as intelligent nanorobots for various biomedical applications in the near future.

Conflicts of interest

The authors declare no competing financial interests.

Acknowledgements

References

1 K. Villa and M. Pumera, Fuel-free light-driven micro/nano-machines: artificial active matter mimicking nature, *Chem. Soc. Rev.*, 2019, **48**, 4966–4978.

2 L. Xu, F. Mou, H. Gong, M. Luo and J. Guan, Light-driven micro/nanomotors: from fundamentals to applications, *Chem. Soc. Rev.*, 2017, **46**, 6905–6926.

3 H. Šípová-Jungová, D. Andrén, S. Jones and M. Käll, Nanoscale inorganic motors driven by light: principles, realizations, and opportunities, *Chem. Rev.*, 2020, **120**, 269–287.

4 D. Xu, Y. Wang, C. Liang, Y. You, S. Sanchez and X. Ma, Self-propelled micro/nanomotors for on-demand biomedical cargo transportation, *Small*, 2019, 1902464.

5 M. Fernández-Medina, M. Ramos-Docampo, O. Hovorka, V. Salgueiriño and B. Städler, Recent advances in nano- and micromotors, *Adv. Funct. Mater.*, 2020, 1908283.

6 J. Wang, R. Dong, H. Wu, Y. Cai and B. Ren, A Review on artificial micro/nanomotors for cancer-targeted delivery, diagnosis and therapy, *Nano-Micro Lett.*, 2020, **12**, 11.

7 F. Novotný, H. Wang and M. Pumera, Nanorobots: machines squeezed between molecular motors and micro-motors, *Chem*, 2020, **6**, 1–18.

8 T. Xu, W. Gao, L. Xu, X. Zhang and S. Wang, Fuel-free synthetic micro-/nanomachines, *Adv. Mater.*, 2017, **29**, 1603250.

9 S. Wang, X. Liu, Y. Wang, D. Xu, C. Liang, J. Guo and X. Ma, Biocompatibility of artificial micro/nanomotors for use in biomedicine, *Nanoscale*, 2019, **11**, 14099–14112.

10 M. Xuan, Z. Wu, J. Shao, L. Dai, T. Si and Q. He, Near infrared light-powered Janus mesoporous silica nano-particle motors, *J. Am. Chem. Soc.*, 2016, **138**, 6492–6497.

11 Z. Deng, F. Mou, S. Tang, L. Xu, M. Luo and J. Guan, Swarming and collective migration of micromotors under near infrared light, *Appl. Mater. Today*, 2018, **13**, 45–53.

12 L. Kong, C. Mayorga-Martinez, J. Guan and M. Pumera, Photocatalytic micromotors activated by UV to visible light for environmental remediation, micropumps, reversible assembly, transportation, and biomimicry, *Small*, 2019, 1903179.

13 K. Rao, F. Li, L. Meng, H. Zheng, F. Cai and W. Wang, A force to be reckoned with: a review of synthetic microswimmers powered by ultrasound, *Small*, 2015, **11**, 2836–2846.

14 T. Xu, L. Xu and X. Zhang, Ultrasound propulsion of micro-/nanomotors, *Appl. Mater. Today*, 2017, **9**, 493–503.

15 M. Pal, N. Somalwar, A. Singh, R. Bhat, S. Eswarappa, D. Saini and A. Ghosh, Maneuverability of magnetic nano-motors inside living cells, *Adv. Mater.*, 2018, **30**, 1800429.

16 T. Li, J. Li, K. I. Morozov, Z. Wu, T. Xu, I. Rozen, A. M. Leshansky, L. Li and J. Wang, Highly efficient freestyle magnetic nanoswimmer, *Nano Lett.*, 2017, **17**, 5092–5098.

17 J. García-Torres, C. Calero, F. Sagués, I. Pagonabarraga and P. Tierno, Magnetically tunable bidirectional locomotion of a self-assembled nanorod-sphere propeller, *Nat. Commun.*, 2018, **9**, 1663.

18 C. Chen, F. Soto, E. Karshalev, J. Li and J. Wang, Hybrid nanovehicles one machine, two engines, *Adv. Funct. Mater.*, 2019, **29**, 1806290.

19 V. Asunción-Nadal, B. Jurado-Sánchez, L. Vázquez and A. Escarpa, Magnetic fields enhanced the performance of tubular dichalcogenide micromotors at low hydrogen peroxide levels, *Chem. – Eur. J.*, 2019, **25**, 13157–13163.

20 Y. Xing, M. Zhou, X. Du, X. Li, J. Li, T. Xu and X. Zhang, Hollow mesoporous carbon@Pt Janus nanomotors with dual response of H$_2$O$_2$ and near-infrared light for active cargo delivery, *Appl. Mater. Today*, 2019, **17**, 85–91.

21 C. Chen, S. Tang, H. E. Karshalev, F. Zhang, J. Li, F. Mou, Y. Liang, J. Guan and J. Wang, Chemical/light-powered hybrid micromotors with "on-the-fly" optical brakes, *Angew. Chem.*, 2018, **130**, 8242–8246.

22 W. Gao, K. M. Manesh, J. Hua, S. Sattayasamitsathit and J. Wang, Hybrid nanomotor: a catalytically/magnetically powered adaptive nanowire swimmer, *Small*, 2011, **7**, 2047–2051.

23 D. Zhou, Y. Gao, J. Yang, Y. Li, G. Shao, G. Zhang, T. Li and L. Li, Light-ultrasound driven collective "firework" behavior of nanomotors, *Adv. Sci.*, 2018, **5**, 1800122.

24 J. Li, T. Li, T. Xu, M. Kiristi, W. Liu, Z. Wu and J. Wang, Magneto-acoustic hybrid nanomotor, *Nano Lett.*, 2015, **15**, 4814–4821.

25 L. Ren, D. Zhou, Z. Mao, P. Xu, J. Huang and T. E. Mallouk, Rheotaxis of bimetallic micromotors driven by chemical-acoustic hybrid power, *ACS Nano*, 2017, **11**, 10591–10598.

26 L. Ren, W. Wang and T. E. Mallouk, Two forces are better than one: combining chemical and acoustic propulsion for enhanced micromotor functionality, *Acc. Chem. Res.*, 2018, **51**, 1948–1956.

27 W. Wang, W. Duan, Z. Zhang, M. Sun, A. Senb and T. E. Mallouk, A tale of two forces: simultaneous chemical and acoustic propulsion of bimetallic micromotors, *Chem. Commun.*, 2015, **51**, 1020–1023.

28 R. Dong, C. Wang, Q. Wang, A. Pei, X. She, Y. Zhang and Y. Cai, ZnO-based microrockets with light-enhanced propulsion, *Nanoscale*, 2017, **9**, 15027–15032.

29 X. Du and S. Qiao, Dendritic silica particles with center-radial pore channels: promising platforms for catalysis and biomedicine applications, *Small*, 2015, **11**, 392–413.

30 A. Maity and V. Polshettiwar, Dendritic fibrous nanosilica for catalysis, energy harvesting, carbon dioxide migation, drug delivery, and sensing, *ChemSusChem*, 2017, **10**, 3866–3913.

31 Y. Wang, X. Du, S. Shi, Z. Liu and H. Lv, Dendritic fibrous nano-particles (DFNPs): rising stars from mesoporous materials, *J. Mater. Chem. A*, 2019, **7**, 5111–5152.

32 H. Lv, Y. Xing, Y. Wang, X. Li, X. Zhang and X. Du, Exploration of accessibility of internal pore surface by using rigid nanoparticles as a probe for constructing the integrated nanocomposites, *J. Alloys Compd.*, 2020, **815**, 152641.

33 Y. Xing, Q. Pan, X. Du, T. Xu, Y. He and X. Zhang, Dendritic Janus nanomotors with precisely modulated coating rates and their effects on velocity, *ACS Appl. Mater. Interfaces*, 2019, **11**, 10426–10433.

34 R. J. Archer, A. J. Parnell, A. I. Campbell, J. R. Howse and S. J. Ebbens, A Pickering emulsion route to swimming active Janus colloids, *Adv. Sci.*, 2018, **5**, 1700528.

35 Y. Liu, R. Dai, Q. Wei, W. Li, G. Zhu, H. Chi, Z. Guo, L. Wang, C. Cui, J. Xu and K. Ma, Dual-functionalized Janus mesoporous silica nanoparticles with active targeting and charge reversal for synergistic tumor-targeting therapy, *ACS Appl. Mater. Interfaces*, 2019, **11**, 44582–44592.

36 K. Lebdioua, A. Aimable, M. Cerbelaud, A. Videcoq and C. Peyratout, Influence of different surfactants on Pickering emulsions stabilized by submicronic silica particles, *J. Colloid Interface Sci.*, 2018, **520**, 127–133.

37 S. Ramadan, L. Guo, Y. Li, B. Yan and W. Lu, Hollow copper sulfide nanoparticle-mediated transdermal drug delivery, *Small*, 2012, **8**, 3143–3150.

38 X. Liu, B. Li, F. Fu, K. Xu, R. Zou, Q. Wang, B. Zhang, Z. Chen and J. Hu, Facile synthesis of biocompatible cysteine-coated CuS nanoparticles with high photothermal conversion efficiency for cancer therapy, *Dalton Trans.*, 2014, **43**, 11709–11715.

39 D. Wang, H. Dong, M. Li, Y. Cao, F. Yang, K. Zhang, W. Dai, C. Wang and X. Zhang, Erythrocyte-cancer hybrid membrane camouflaged hollow copper sulfide nanoparticles for prolonged circulation life and homotypic-targeting photothermal/chemotherapy of melanoma, *ACS Nano*, 2018, **12**, 5241–5252.

40 R. Wang, Z. He, P. Cai, Y. Zhao, L. Gao, W. Yang, Y. Zhao, X. Gao and F. Gao, Surface-functionalized modified copper sulfide nanoparticles enhance checkpoint blockade tumor immunotherapy by photothermal therapy and antigen capturing, *ACS Appl. Mater. Interfaces*, 2019, **11**, 13964–13972.

41 M. Wu, T. Mei, C. Lin, Y. Wang, J. Chen, W. Le, M. Sun, J. Xu, H. Dai, Y. Zhang, C. Xue, Z. Liu and B. Chen, Melanoma cell membrane biomimetic versatile CuS nanoprobes for homologous targeting photoacoustic imaging and photothermal-chemotherapy, *ACS Appl. Mater. Interfaces*, 2020, **12**(14), 16031–16039.